

# Fragmentation of protoplanetary disks around M-dwarfs

Isaac Backus,<sup>1</sup><sup>★</sup> Thomas Quinn,<sup>1</sup><sup>†</sup>

<sup>1</sup>University of Washington, Seattle, WA 98195, USA

Accepted XXX. Received YYY; in original form ZZZ

## ABSTRACT

We investigate the conditions required for planet formation via gravitational instability (GI) and protoplanetary disk (PPD) fragmentation around M-dwarfs. Using a suite of 64 SPH simulations with  $10^6$  particles, the parameter space of disk mass, temperature, and radius is explored, bracketing reasonable values based on theory and observation. Our model consists of an equilibrium, gaseous, and locally isothermal disk orbiting a central star of mass  $M_* = M_\odot/3$ . Disks with a minimum Toomre  $Q$  of  $Q_{min} \lesssim 0.9$  will fragment and form gravitationally bound clumps. Some previous literature has found  $Q_{min} < 1.3 - 1.5$  to be sufficient for fragmentation. Increasing disk height tends to stabilize disks, and when incorporated into  $Q$  as  $Q_{eff} \propto Q(H/R)^\alpha$  for  $\alpha = 0.18$  is sufficient to predict fragmentation. Some discrepancies in the literature regarding  $Q_{crit}$  may be due to different methods of generating initial conditions (ICs). A series of 15 simulations demonstrates that perturbing ICs slightly out of equilibrium can cause disks to fragment for higher  $Q$ . Our method for generating ICs is presented in detail. We argue that GI likely plays a role in PPDs around M-dwarfs and that disk fragmentation at large radii is a plausible outcome for these disks.

**Key words:** accretion, accretion disks – protoplanetary disks – methods: numerical

## 1 INTRODUCTION

The importance of gravitational instabilities (GI) in the evolution of protoplanetary disks (PPDs) and in planet formation remains hotly debated (Cameron 1978; Boss 1997; Durisen et al. 2007; Boley & Durisen 2010; Paardekooper 2012). In recent years, the core accretion (CA) plus gas capture model of giant planet formation has received much attention (Pollack et al. 1996; Helled et al. 2014), but GI is still seen as a candidate for the direct formation of giant planets, especially at large orbital radii (Boley 2009). While CA gives a more natural explanation of terrestrial planet formation and small bodies, GI may be important for the formation of these objects via solid enhancement within spiral arms or fragments (Haghighipour & Boss 2003). GI may also play an important role during the embedded phase of star formation (Vorobyov 2011).

Understanding the role of GI in planet formation will require continued observation of PPDs (Andrews & Williams 2005; Isella et al. 2009; Mann et al. 2015) and further theoretical work. Of primary importance are (i) disk cooling times (Gammie 2001; Rafikov 2007; Meru & Bate 2011, 2012), which must be sufficiently short to allow density per-

turbations to grow against pressure support, and (ii) the Toomre  $Q$  parameter (Toomre 1964):

$$Q \equiv \frac{c_s \kappa}{\pi G \Sigma} \quad (1)$$

where  $c_s = \sqrt{\gamma k_B T / m}$  is the gas sound speed,  $\kappa$  is the epicyclic frequency ( $\kappa = \Omega$  for a massless disk), and  $\Sigma$  is the disk surface density. As  $Q$  decreases toward unity, PPDs become increasingly unstable, and if  $Q$  becomes sufficiently small, disks will undergo fragmentation.

The parameters required for fragmentation, such as disk mass ( $M_d$ ), disk radius ( $R_d$ ), and disk temperature ( $T$ ), are constrained by the critical  $Q$  required for fragmentation. Some previous studies have found values of  $Q_{crit} = 1.3 - 1.5$  (Boss 1998, 2002; Mayer et al. 2004), although it has been noted that  $Q$  can drop below unity and the disk may still tend to a self-regulating state (Boley 2009).

Determining parameters required for fragmentation is complicated by issues of resolution. The constant ( $\beta$ ) cooling simulations of Meru & Bate (2011) demonstrated non-convergence of SPH simulations. Further work (Meru & Bate 2012; Rice et al. 2012) suggested artificial viscosity is to blame. Work is underway to investigate this problem; however, resolution dependent effects are still poorly understood in SPH simulations of PPDs (Rice et al. 2014).

Previous work has tended to focus on PPDs around so-

<sup>★</sup> E-mail: ibackus@gmail.com

<sup>†</sup> E-mail: trq@astro.washington.edu

lar mass stars. Motivated by the large population of low mass stars, we study GI around M-dwarfs with mass  $M_* = M_\odot/3$ . Around 10% of known exoplanets are around M-dwarfs (Han et al. 2014). Due to selection effects of current surveys such as Kepler (Borucki et al. 2010), this is expected to be a large underestimate of the actual population. Recent discoveries show that disks around M and brown dwarfs are different from those around solar analogs: the mass distribution falls off more slowly with radius, and is denser at the midplane. These differences change disk chemistry and the condensation sequence. M-dwarf disks are also less massive and survive longer (Apai & Pascucci 2009, 2010). Core accretion timescales, which scale as the orbital period, are long around M-dwarfs. Because the stars are much lower in luminosity, their disks are substantially cooler. Additionally, planets orbiting nearby M-dwarfs are likely to be the first smaller planets spectroscopically characterized (Seager et al. 2015).

The simulations of Boss (2006a) indicate that GI is able to form gas giants around M-dwarfs. Boss (2006b) and Boss (2008) even argue that super earths around M-dwarfs can be explained as gas giants, formed via GI, and stripped of their gaseous envelopes by photoevaporation.

In this paper we explore the conditions required for disk fragmentation under GI around M-dwarfs. Previous studies have found a range of values of the  $Q_{crit}$  required for disk fragmentation (Boss 1998, 2002; Mayer & Gawryszczak 2008; Boley 2009). Discrepancies may be due to different equations of state (EOS), cooling algorithms, numerical issues such as artificial viscosity prescriptions, Eulerian vs. Lagrangian codes, and initial conditions (ICs). ICs close to equilibrium are non-trivial to produce and so we explore the dependence on ICs of simulations of gravitationally unstable disks.

We focus on probing disk fragmentation around M-Dwarfs, which remains poorly studied, and the importance of ICs. These warrant a simple, well understood isothermal EOS. We therefore probe the Toomre  $Q$  required for fragmentation while leaving the question of the cooling required for fragmentation for future work.

We begin in §2 by presenting our method for generating equilibrium initial conditions for smoothed-particle hydrodynamic (SPH) simulations of PPDs, with particular care taken in calculating density and velocity profiles. §3 describes the suite of simulations presented here and discuss the theoretical and observational motivations behind our disk profiles. §4 presents our analysis of disk fragmentation around M-dwarfs and discusses the importance of ICs in simulations of unstable disks. §5 presents our method for finding and tracking gravitationally bound clumps and discusses clump formation in our simulations. We present our discussion in §6. We consider the effects of thermodynamics and ICs on fragmentation in PPD simulations and argue that GI should play an important role in PPDs around M-dwarfs and that we expect disk fragmentation at large radii to occur around many M-dwarfs.

## 2 INITIAL CONDITIONS

A major emphasis of this work was to ensure that ICs were as close to equilibrium as possible. Axisymmetric disks very

near equilibrium may not realistically model actual PPDs, but we wish to make as few assumptions as possible about disks and have attempted to minimize numerical artifacts. One worry is that disks too far from equilibrium may artificially enter the non-linear regime, possibly initiating fragmentation in an otherwise stable disk. This possibility is explored in §4.1. In this section, we present our method for generating ICs.<sup>1</sup>

Many methods have been used in previous work for generating initial conditions. As discussed by Mayer & Gawryszczak (2008), apparently contradictory results in fragmentation studies may be due to differences in ICs used. Much published research does not detail IC generation in sufficient detail to be reproducible, but we can sketch out a few different approaches used. Boss (1998) developed ICs by defining the midplane density  $\rho(R, z = 0)$ , analytically estimating  $\rho(z)$ , using an approximate circular velocity, and iteratively adjusting the temperature profile to create a steady state solution.

As with us, other authors (Mayer et al. 2004; Rogers & Wadsley 2011) were able to define the surface density and temperature profiles. They then estimated vertical hydrostatic equilibrium to calculate density. Mayer et al. (2004) estimated the gas velocity required for circular orbits ( $v_{circ}$ ) from gravitational forces and adjusted for hydrodynamic forces. Additionally, as with others (e.g. Mayer & Gawryszczak (2008)), they also approached low  $Q$  values by slowly growing the disk mass. Similarly, Boley (2009) used low mass, high- $Q$  models in his grid code simulations and accreted mass from the  $z$  boundaries gradually to grow simulations towards instability.

Pickett et al. (2003) placed great care in developing equilibrium ICs. In contrast to our ICs, they also modeled the central, accreting star. They generated a stable disk ( $Q = 1.8$ ) using a field equilibrium code (Hachisu 1986). They specified the specific angular momentum  $j(R)$  of the gas (which forces velocity to be solely a function of radius) then iteratively used a self consistent field method to solve the Poisson gravity equation and balance the hydrodynamic forces to approach equilibrium. A shooting method for  $j(R)$  was used to reach a desired  $\Sigma(R)$ . For low- $Q$  simulations, they cooled the disk until it reached  $Q_{min} = 0.9$ .

For our simulations, we desired to scan parameter space by defining surface density ( $\Sigma$ ) and temperature ( $T$ ) radial profiles, along with star mass. From these, the gas density ( $\rho$ ) can be estimated to ensure vertical hydrostatic equilibrium in the disk. SPH particles are then semi-randomly seeded and their equilibrium circular velocities are estimated using the NBody/SPH simulation code ChaNGa to calculate the forces. Our method allows us to directly and quickly generate equilibrium ICs for low  $Q$  values and arbitrary  $\Sigma$  and  $T$  profiles.

### 2.1 Estimating $\rho(R, z)$

To estimate  $\rho(R, z)$ , we first define  $M_*$ ,  $\Sigma(R)$ , and  $T(R)$ . Hydrostatic equilibrium is solved by adjusting the vertical density

<sup>1</sup> Our code for generating ICs is freely available on github at <https://github.com/ibackus/diskpy> as a part of our PPD python package *diskpy*

profile to maintain vertical hydrostatic equilibrium and adjusting the gas orbital velocity to ensure radial equilibrium.

To be in equilibrium along the vertical direction, the vertical component of gravity from the star and the disk's self-gravity should balance the vertical pressure gradient in the gas. For the disk self-gravity term, we assume the thin disk approximation where  $\rho$  is assumed to be only a function of  $z$ .  $T$  is set to be independent of  $z$ , which is reasonable for the locally isothermal equation of state used in these simulations. All quantities are axisymmetric and symmetric about the midplane  $z = 0$ . Under these assumptions, the vertical hydrostatic equilibrium condition can be written as:

$$\frac{k_B T}{m} \frac{d\rho}{dz} + \frac{GM_* z \rho}{(z^2 + R^2)^{3/2}} + 4\pi G \rho \int_0^z \rho(z') dz' = 0 \quad (2)$$

where  $m$  is the mean molecular weight of the gas,  $M_*$  is the star's mass and  $R$  is the cylindrical radius. The first term is the pressure gradient and would be altered for a non-isothermal EOS. The boundary conditions are:

$$\int_0^\infty \rho(z') dz' = \Sigma/2 \quad (3a)$$

$$\left. \frac{d\rho}{dz} \right|_{z=0} = 0 \quad (3b)$$

To apply these boundary conditions, eq.(2) is transformed to be a differential equation for  $I(z) \equiv \int_z^\infty \rho(z') dz'$ , which gives an equation of the form:

$$\frac{d^2 I}{dz^2} + \frac{dI}{dz} \left[ \frac{c_1 z}{(z^2 + R^2)^{3/2}} + c_2 \left( \frac{\Sigma}{2} - I \right) \right] = 0 \quad (4)$$

with the constants set by eq.(2). Then eq.(4) is solved numerically by a root finding algorithm. The density is calculated by applying  $\rho = -\frac{dI}{dz}$ . To ensure a robust solution, the solution for  $\rho$  is then iteratively entered into a root finding algorithm for eq.(2) and rescaled to ensure the boundary condition in eq.(3a) is met.<sup>2</sup>

## 2.2 Generating particle positions

The solution to  $\rho$  is then used to semi-randomly seed SPH particles. To mitigate Poisson noise, we used the method of Cartwright et al. (2009a) which places the particles along a spiral in the  $x - y$  plane to keep them more evenly spaced. The spiral is made in such a way that  $\Sigma(R)$  is reproduced. See Cartwright et al. (2009a) for a more detailed explanation. The particle  $z$  values are then randomly assigned according to  $\rho(z)$ . Note that it is important to make the spirals trailing (rather than leading) to avoid unwinding effects and swing amplification.

## 2.3 Circular velocity calculation

A major concern with avoiding artifacts in the ICs is calculating the particle velocities required for circular orbits

( $v_{circ}$ ). For typical disks,  $v_{circ}$  is one to two orders of magnitude larger than  $c_s$ . Thus, particle velocities which deviate from  $v_{circ}$  on the percent level will deposit a significant amount of power into the disk. If this dominates the available thermal energy (which tends to stabilize the disk), the disk may enter a non-linear regime and fragment for unrealistically high  $Q$ . We include a demonstration of this in §4.1.

To calculate  $v_{circ}$ , we employ our simulation code ChaNGa to calculate the radial gravitational and hydrodynamical forces on all particles. Following Mayer et al. (2004), we set the gravitational softening length to  $\epsilon_s = 0.5 \langle h \rangle$ , where  $\langle h \rangle$  is the SPH smoothing length, calculated over the 32 nearest neighbors, and averaged over all particles in the simulation. The softening length for the star is set as the distance to the nearest gas particle. ChaNGa is then used to estimate the gravitational and SPH forces separately.

To deal with SPH noise, the radial forces must be averaged over many particles. The gravitational and SPH forces are averaged separately because of a different dependence on position. In both cases, 50 radial bins are used. To fit the  $R$  and  $z$  dependence of the gravitational forces, particles are binned radially, and for each bin a line is fit to the radial force per mass due to gravity, as a function of  $\cos \theta$ :

$$a_{g,i}(\cos \theta) = m_i \cos \theta + b_i \quad (5)$$

where  $\theta$  is the angle above the plane of the disk. Here  $\cos \theta$  is chosen as the independent variable because the radial gravitational force from the central star is proportional to  $\cos \theta$ . The fit parameters ( $m_i, b_i$ ) are then linearly interpolated as a function of  $R$  to calculate  $a_g(R, z)$ .

The radial hydrodynamic forces display very little  $z$  dependence, as is expected for a temperature profile independent of  $z$ . The SPH forces are averaged over logarithmically spaced radial bins and then interpolated with a linear spline. From the total force per mass ( $a = a_{grav} + a_{SPH}$ ) we can calculate  $v_{circ}$  as:

$$v_{circ} = \sqrt{aR} \quad (6)$$

## 3 SET OF RUNS

### 3.1 ChaNGa

All the simulations in this paper were performed with ChaNGa<sup>3</sup>, a highly parallel N-body/SPH code originally written for cosmology simulations (Menon et al. 2015). ChaNGa is written in the CHARM++ parallel programming language which allows the overlap of computation and communication, and enables scaling to over half a million processor cores (Menon et al. 2015). The physics modules of ChaNGa are taken from GASOLINE (Wadsley et al. 2004) where gravity is calculated using a Barnes-Hut (Barnes & Hut 1986) tree with hexadecapole expansions of the moments, and hydrodynamics is performed with SPH. All the simulations performed here used a gravitational force accuracy (node opening) criterion of  $\theta_{BH} = 0.7$ . Timesteps are set by a Courant condition of  $\eta_C = 0.3$  and an acceleration

<sup>2</sup> The current publicly available version of our code *diskpy* uses an altered version of this algorithm to solve eq. 2 which is significantly faster and has been tested to provide the same results as the algorithm described here.

<sup>3</sup> A public version of ChaNGa can be downloaded from <http://www-hpcc.astro.washington.edu/tools/changa.html>

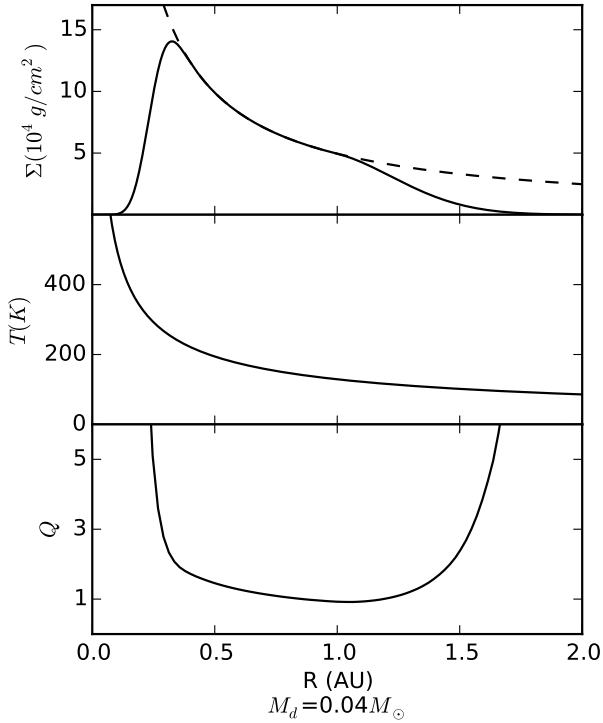


**Figure 1.** Example radial profiles for powerlaw surface density  $\Sigma \propto 1/R$ , with  $R_m = 0.3$  AU and  $R_d = 1$  AU. **Top:** Surface density profile including cutoffs (solid) and excluding cutoffs (dashed). **Middle:** Disk temperature  $T \propto R^{-0.59}$  **Bottom:** Toomre  $Q$ , calculated including full disk self gravity, SPH forces, and calculation of  $\kappa$ .

criterion of  $\Delta t_i = \eta \sqrt{\frac{\epsilon_i}{a_i}}$  where  $\epsilon_i$  and  $a_i$  are respectively the softening and acceleration of a particle, and  $\eta = 0.2$ . To stabilize the SPH we use the Monaghan (1992) artificial viscosity with coefficients  $\alpha = 1$  and  $\beta = 2$ , and we use the Balsara (1995) switch to suppress viscosity in non-shocking shearing environments. We have tested ChaNGa with the PPD Wengen code test 4 and it performs well (see Appendix A). The simulations presented here each took about 3k core-hours running on eight 12-core nodes on the University of Washington’s supercomputer Hyak.

### 3.2 Disk Profiles

Figures 1 & 2 show radial profiles for example simulations. Pictured are  $\Sigma(R)$  (top panel),  $T(R)$  (middle panel), and  $Q(R)$  (bottom panel). The exact disk structure of PPDs, especially young ones, is poorly constrained. Therefore we adopt simple, easy to interpret profiles, and consider a range of values of  $M_d$  and  $T$  in order to bracket plausible disk parameters. Below we describe our choice of disk temperature and surface density profiles, along with the theoretical and observational motivations for them.

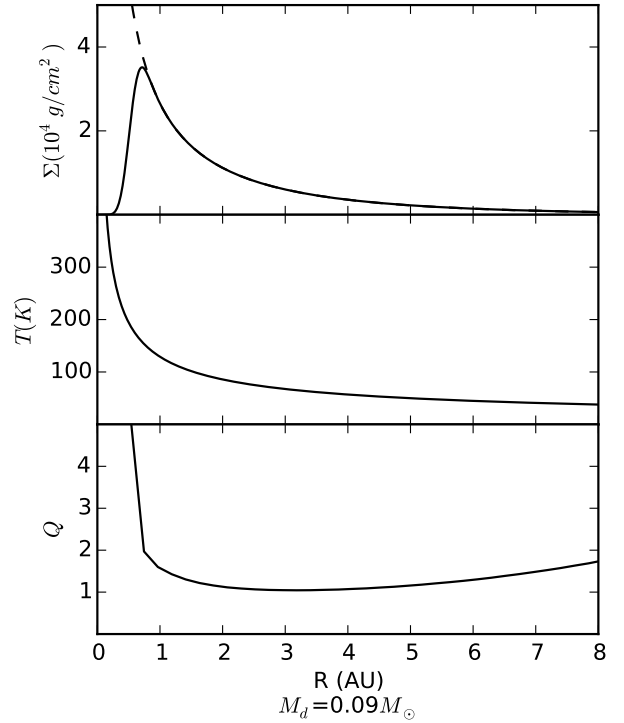


**Figure 2.** Example radial profiles for a viscous disk surface density  $\Sigma(r) = \Sigma_0 r^{-\gamma} \exp(-r^2/\gamma)$ , where  $r$  is a dimensionless radius and  $\gamma = 0.9$ . The radius containing 95% of the mass is  $R_d = 11$  AU. **Top:** Surface density profile including cutoffs (solid) and excluding cutoffs (dashed). **Middle:** Disk temperature  $T \propto R^{-0.59}$  **Bottom:** Toomre  $Q$ .

#### 3.2.1 Temperature

For a blackbody disk with heating dominated by solar radiation, Chiang & Goldreich (1997) showed that the temperature profile should be a power law. The exponent is  $q = 3/7$  for a fully flared disk and  $q = 3/4$  for a flat disk. We therefore adopt a temperature profile of the form:

$$T(R) = T_0 \left( \frac{R}{R_0} \right)^{-q} \quad (7)$$

where  $R_0$  was set to be 1 AU and  $T_0$  is the temperature at 1 AU. The values we adopt for  $T_0$  and  $q$  come from the observations of Andrews & Williams (2005). They observed dust SEDs of circumstellar disks in the Taurus-Auriga star forming region. Fit results for 44 mainly solar type stars yielded median inferred parameters of  $T_0 = 148K$  and  $q = 0.58$  (see their Table 2). Averaging their results for M-Stars only, we adopt  $q = 0.59$  for every simulation and  $T_0 = 130K$  as our central fiducial values. This power law of  $q = 0.59$  lies between a fully flared and completely flat disk. Given the uncertainty of these values we also ran simulations with  $T_0 = 65K$  and  $260K$  to bracket plausible disk temperatures.

#### 3.2.2 Surface density

Two functional forms for  $\Sigma$  were used: a power law (Fig. 1) and the similarity solution for a thin, viscous disk (Fig. 2).

The power law used was:

$$\Sigma(R) = \Sigma_0 \left( \frac{R}{R_0} \right)^{-1} \quad (8)$$

Where the normalization  $\Sigma_0$  is fixed by the desired disk mass. As shown in Fig. 1, interior and exterior cutoffs were applied. For  $R > R_d$ , an exponential cutoff was applied by multiplying  $\Sigma(R)$  in eq.(8) by:

$$\Sigma_{\text{exterior}} = \Sigma(R) e^{-(R-R_d)^2/L^2} \quad (9)$$

where the cutoff length was set to  $L = 0.3R_d$ . This form ensures that  $\Sigma$  and  $\frac{d\Sigma}{dR}$  are unchanged at  $R = R_d$ . The interior cutoff was applied by multiplying  $\Sigma$  by a smooth high order polynomial approximation to a step function, defined to be  $[0, 1]$  at  $R = [0, R_{\text{cut}}]$  with the first 10 derivatives set to be 0 at  $R = [0, R_{\text{cut}}]$ . For these simulations  $R_{\text{cut}} = 0.5R_d$  and  $\Sigma$  differs significantly from a power law for  $R \lesssim 0.3R_d$  (see Fig.1). This radius was chosen such that: (a)  $Q \gg 1$  at  $R_{\text{cut}}$  to ensure the disk is stable at  $R_{\text{cut}}$ , and (b) the cutoff is applied far enough from the most unstable disk region and removes little enough mass that fragmentation should not be strongly affected by the cutoff.

The second functional form for  $\Sigma$  (see Fig.2) comes from the similarity solution to a thin, light, viscous disk orbiting a star, as found in Lynden-Bell & Pringle (1974). For a viscosity obeying a power law  $\nu \propto R^\gamma$ , at a given time  $\Sigma$  can be written as:

$$\Sigma(r) = \Sigma_0 r^{-\gamma} \exp(-r^{2-\gamma}) \quad (10)$$

where  $r$  is a dimensionless radius and the normalization  $\Sigma_0$  is fixed by the disk mass. Note that the full similarity solution includes a time dependence which we fold into  $\Sigma_0$  and  $r$ . From fits to observations of 9 circumstellar disks, Andrews et al. (2009) found a median value of  $\gamma = 0.9$ , which is the value we adopt here. For this profile, no exterior cutoff is required. The same interior cutoff as for the power law  $\Sigma$  was applied at  $r = 0.1$ .

If we define  $R_d$  to be the radius containing 95% of the disk mass (ignoring the interior cutoff), then:

$$r = \frac{R}{R_d} \ln(1/0.05)^{1/(2-\gamma)} \quad (11)$$

As has been noted before (e.g. Isella et al. (2009)), there is no physical motivation for adopting a power law for  $\Sigma$ . It is also not clear how applicable the viscous profile is. These are just simple functional forms often adopted in previous work. We have examined the end state of high- $Q$  runs and they are better approximated by the viscous profile, but the fit is not perfect.

### 3.3 Run Parameters

For a given functional form of  $\Sigma(R)$  and  $T(R)$ , three parameters must be set to make our ICs and thereby fix a value of  $Q_{\text{min}}$ : the temperature normalization ( $T_0$ ), the disk mass ( $M_d$ ), and the disk radius ( $R_d$ ). The choices of  $T_0$  are discussed in §3.2.1.

#### 3.3.1 Disk mass

Under our scheme, setting  $M_d$  fixes the surface density normalization. We selected plausible values to explore, ranging

from 0.01 to  $0.08M_\odot$ . Isella et al. (2009) reported observations of 11 disks around pre-main-sequence stars, including 7 around M-stars. From their Tables 1 & 2, we find a median value of  $M_d/M_* = 0.15$ , which for our simulations ( $M_* = 1/3M_\odot$ ) gives a central value of  $M_d = 0.05M_\odot$ . It should be stressed that these disk masses are inferred using an assumed gas to dust ratio of 100 and therefore may have large, uncharacterized uncertainties.

#### 3.3.2 Disk radius

Isella et al. (2009) argue that for a typical disk,  $R_d$  increases from around 20 AU to 100 AU over the course of  $\sim 5$  Myr. This tends to stabilize disks by decreasing  $\Sigma$  over time. Since we are interested in disks at their most unstable, we adopt 20 AU as our central fiducial value. To explore parameter space, we used values of  $R_d$  ranging from 1/3 AU to 30 AU.

#### 3.3.3 Numerical Parameters

For the analysis of fragmentation criteria, a set of 64 ICs were run with  $10^6$  particles. For typical disks, this yields particles with a mass of  $m_{\text{particle}} \approx 5 \times 10^{-5} M_{\text{Jupiter}}$ . A locally isothermal EOS with a mean molecular weight of 2 was used for the gas. Following Mayer et al. (2004), we set the gravitational softening length to  $\epsilon_s = 0.5 \langle h \rangle$ , where  $\langle h \rangle$  is the SPH smoothing length calculated over the 32 nearest neighbors and averaged over all particles. Typical values are around  $\langle h \rangle = 5 \times 10^{-3} R_d$ .

The central star (mass  $M_\odot/3$ ) was set to be a sink particle: when a gas particle approaches the star within a distance of  $R_{\text{sink}}$ , its mass and momentum are accreted onto the star.  $R_{\text{sink}}$  was set as the distance to the closest gas particle in the ICs. This yielded  $R_{\text{sink}} = [0.08R_d, 0.02R_d]$  for the power law and viscous  $\Sigma$  profiles, respectively.

Making the central star a sink serves two purposes worth mentioning. A gas particle near the star gains a large velocity, experiences strong forces, and is often captured in a tight orbit around the star. This requires a very small time-step which can increase computation time by orders of magnitude. Secondly, the adaptive time-stepping used by ChaNGa can fail to conserve momentum when two interacting particles require time-steps which differ by more than a couple orders of magnitude. This momentum non-conservation is particularly problematic for tight, rapid orbits. The effect is sufficiently strong that very stable disks ( $Q > 2$ ) were seen to fragment when the central star was not treated as a sink.

We note that treating the star as a sink in this manner is unrealistic in that accretion happens at very large radii (of order an AU). When accretion happens, the star will jump to the center of mass of the star + particle system. In the limit of low accretion rates and in locations far from the star this will be a negligible effect, but in disks with high accretion a different scheme should be used. For our simulations there is very little accretion: less than  $10^{-3} M_d$  over the duration of the simulations.

As shown in figure 5, non-fragmenting simulations were run for  $\sim 30$  outer rotational periods (ORP), where we define 1 ORP as the orbital period at the most unstable disk radius. ORPs for our disks range from 0.3 yrs for our smallest

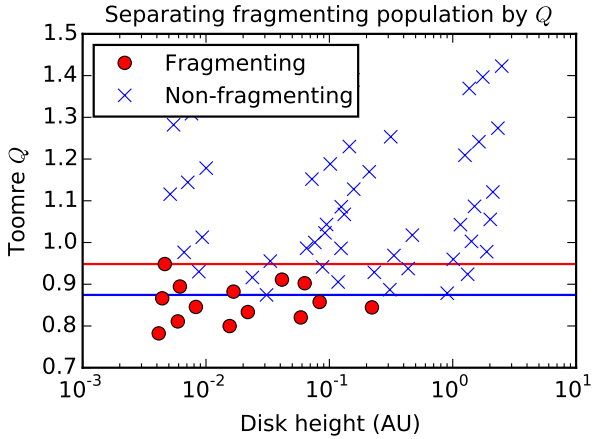


**Figure 3.** Minimum Toomre  $Q$  for the fragmenting (clump-forming) and non-fragmenting simulations. The red (blue) lines mark the largest (smallest) values of the fragmenting (non-fragmenting) simulations. The two populations overlap around  $Q \approx 0.9$ .

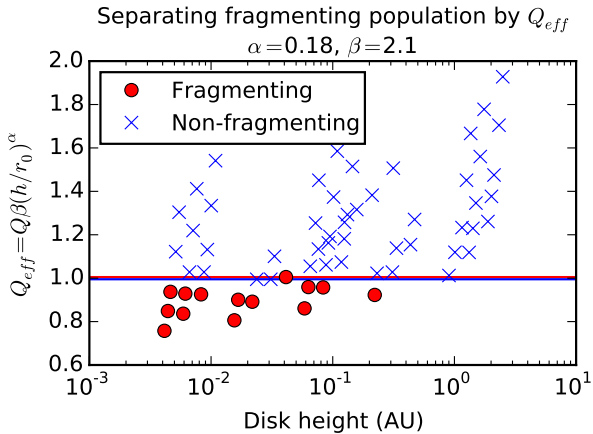


**Figure 4.** Minimum effective Toomre  $Q$  ( $Q_{eff}$ ) for the fragmenting (clump-forming) and non-fragmenting simulations. Re-parameterizing the stability criterion for a protoplanetary disk as  $Q_{eff} = Q\beta(H/R)^\alpha$  is sufficient for predicting whether a protoplanetary disk will fragment.  $\beta$  is a normalization factor chosen such that disks with a  $Q_{eff} < 1$  will fragment.

disks to 300 yrs for the largest. Disks with parameters close to fragmentation were run longer (100–200 ORP) to ensure they reached a steady state which would not fragment. Since the main goal of this work is to investigate fragmentation of PPDs and since computation time increases drastically after clump formation, simulations which fragmented were run for around 1–2 ORP after fragmentation. Figure 5 shows the fragmentation timescales for these disks.

#### 4 FRAGMENTATION ANALYSIS

The primary goal of this paper is to investigate under what conditions we can expect a PPD surrounding an M-dwarf to fragment. The parameters explored by our model are  $T$ ,  $M_d$ , and  $\Sigma$ . Although all simulations were run with a star of  $M_* = M_\odot/3$ , we also extend our analysis to stars of similar mass. As expected, we find sufficiently heavy or cold disks will fragment under GI.

Gravitational instability in PPDs is typically parameterized by the Toomre  $Q$  parameter (eq. 1). For our isothermal simulations,  $c_s = \sqrt{k_B T/m}$ . Two dimensional disks will be unstable for  $Q > 1$ , but the instability and fragmentation criteria for 3D disks remain uncertain. Previous studies have found that 3D disks will fragment for  $Q_{min}$  significantly greater than 1 (Boss 1998, 2002; Mayer et al. 2004; Durisen et al. 2007); however, we do not find this to be the case for our simulations. Figure 3 shows the fragmentation boundary for our simulations. Disks with  $Q \lesssim 0.9$  fragment. Here, we define fragmentation to be when the first gravitationally bound clump is found (see §5).

We also considered the effects of swing amplification. If the parameter:

$$X_m = \frac{\kappa^2 R}{2\pi G \Sigma} \frac{1}{m} \quad (12)$$

is near or below unity, small leading disturbances will amplify upon becoming trailing disturbances and can drive disk dynamics, especially spiral arm growth (Binney & Tremaine 1987). Lower order modes are expected to dominate. For our disks, our lowest value is  $X_1 = 5.7$ , and most disks have  $X_1 > 10$ , so swing amplification should not be significant in these simulations.

Another proposed instability in gaseous disks is provided by the SLING mechanism (Adams et al. 1989; Shu et al. 1990), which is driven by  $m = 1$  mode growth and is sensitive to the outer edge of the disk. For our simulations, we see little  $m = 1$  power. Additionally, we tested the importance of the outer edge by applying a step-function cutoff to  $\Sigma$  on the disk outer edge for marginally stable disks and the overall behavior was unaltered. It therefore seems unlikely that the SLING mechanism plays a major role in these simulations.

It should be noted that for our simulations we calculate  $Q$  from the ICs. Since the equilibrium orbital velocity is known (see §2.3), we can directly calculate  $\kappa^2 = \frac{2\Omega}{R} \frac{d}{dR}(R^2\Omega)$ . This fully includes the effects of a 3D disk with self-gravity and pressure gradients.  $\Sigma$  is calculated by binning SPH particles radially, summing their masses, and dividing by the annulus area. A common approximation for light disks is to ignore disk self gravity and pressure gradients and use  $Q \approx c_s \Omega / \pi G \Sigma$ , which for disks of  $M_d/M_* \approx 0.1$  underestimates  $Q$  at the 10% level. Different estimates of  $Q$  may account for some of the discrepancy in the literature regarding the critical  $Q$  required for fragmentation.

As can be seen in figure 3, there is some overlap in  $Q$  for the fragmenting and non-fragmenting populations. Since the Toomre stability criterion strictly applies to a 2D disk, this is unsurprising. Following the work of Romeo et al. (2010), to higher order a disk scale height correction enters into the dispersion relation for axisymmetric perturbations. Taller disks should be more stable than thinner ones.

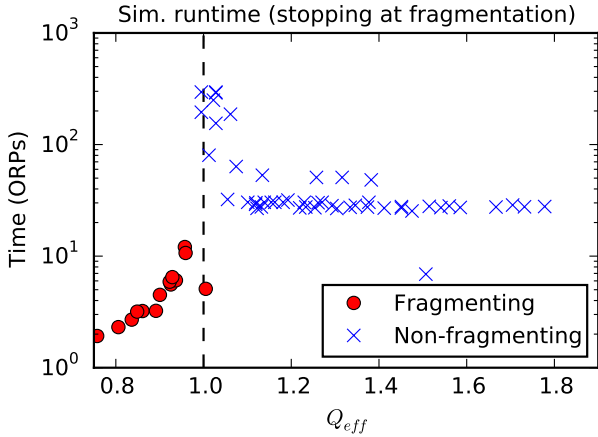


**Figure 5.** Total simulation time (non-fragmenting simulations) and time until fragmentation (fragmenting simulations), in units of the orbital period at the most unstable disk radius. Fragmentation is defined to occur when a gravitationally bound clump forms. The fragmentation timescale increases rapidly as  $Q_{eff}$  approaches 1. Simulations with  $Q_{eff} \geq 1$  were run for longer to verify that they do not fragment.

We re-parameterized  $Q$  to include disk height as:

$$Q_{eff} \equiv Q\beta(H/R)^\alpha \quad (13)$$

where  $H$  is the disk scale height and  $\alpha$  is a free parameter.  $\beta$  is normalization parameter that we set such that  $Q_{eff} < 1$  is the boundary for disk fragmentation (see below).  $H$  is calculated as the standard deviation of the vertical density profile, rather than the first order approximation  $c_s/\Omega$ . We then fit the power law  $\alpha$  to minimize the overlap of the boundaries in  $Q_{eff}$  for the fragmenting/non-fragmenting population. Figure 4 shows the separation of the two populations (compare to fig. 3). For  $\alpha = 0.18$  and  $\beta = 2.1$ , simulations with  $Q_{eff} < 1$  fragment.

A power law was chosen because it is a simple functional form, and there is a great deal of self-similarity in PPDs, but other forms such as linear corrections might be suitable as well. As expected, taller disks have a larger  $Q_{eff}$  and are therefore less prone to fragmentation, although the dependence on height is weak.

We also found that  $Q_{eff}$  correlates strongly with time until fragmentation (see fig. 5). We found it to predict fragmentation time with less scatter than  $Q$ . To verify that  $H/R$  is an important parameter in predicting disk fragmentation, we considered power law dependence of  $Q_{eff}$  on various dimensionless combinations of parameters, including the most unstable wavelength,  $c_s$ ,  $T$ , and  $\Omega$ . We found  $H/R$  to separate the populations most strongly.

These considerations indicate disk scale height is an important parameter in dictating stability and fragmentation. With the fragmentation boundary  $Q_{eff} = 1$ , we are equipped to estimate disk parameters for which we may reasonably expect disks to fragmentation.

Figure 6 shows the boundaries for disk fragmentation for a star of mass  $M_* = M_\odot/3$  as a function of  $R_d$ ,  $M_d$ , and the temperature at 1 AU ( $T_0$ ). The contour lines mark the

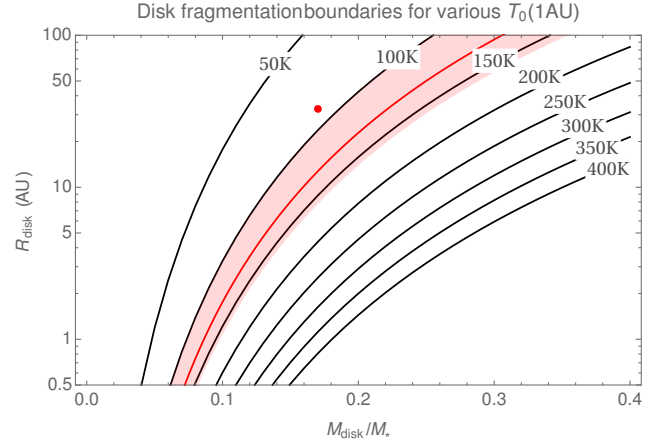


**Figure 6.** Fragmentation criteria for disk ICs. The curved lines define which disks will fragment for various disk temperatures at 1 AU, assuming a temperature profile of  $T \propto r^{-0.59}$  and a surface density profile of  $\Sigma \propto 1/R$ . ICs which lie to the right of a line will fragment. The boundaries are  $Q_{eff} = 1$  contours, where the  $Q_{eff}$  estimates include approximations for disk height and disk self gravity. The red line marks the boundary defined by the fiducial temperature of  $T_0(1 \text{ AU}) = 130 \pm 25 \text{ K}$  from Andrews & Williams (2005) and the red dot marks the fiducial disk mass and radius for a young disk from Isella et al. (2009) (see §3.3 for a discussion of these values). These fiducial values likely have large uncertainties (not pictured).

boundary for various values of  $T_0$ . Disks to the right of the contour lines have a minimum  $Q_{eff} < 1$  and will fragment.

The red boundary marks the fiducial value of  $T_0 = 130 \text{ K}$  from the observations of Andrews & Williams (2005) (see §3.2.1), with the surrounding red region marking the sample scatter in their observations of 25K. The red point marks the fiducial values (for a young disk) of  $M_d$  and  $R_d$  from the observations of Isella et al. (2009) (see §3.2.2).

Since the fiducial disk parameters lie to the left of the fiducial boundary, we expect the observed disks to not be susceptible to fragmentation by GI. This is to be expected, since the timescales for fragmentation are so much shorter than observed disk lifetimes/ages, it is unlikely to observe gravitationally highly unstable PPDs. However, we note that observed disk parameters lie close to the region of fragmentation.

#### 4.1 Sensitivity to ICs

It is important to understand the causes of disk fragmentation in our simulations. We have paid particular care to characterize numerical issues which may drive fragmentation. In appendix B we present a simple convergence test which demonstrates that for our locally isothermal SPH treatment, lower resolution disks fragment more easily.

To assess the sensitivity of disk fragmentation to the state of the ICs, we applied a series of small perturbations to disks close to the fragmentation boundary, with a  $Q_{eff}$  slightly greater than 1. We used two of the ICs in our suite of runs which didn't fragment: one with  $Q_{eff} = 1.01$  and one with  $Q_{eff} = 1.12$  (simulations 2 and 5 in table B2). We found that perturbing orbital velocities slightly out of equilibrium

**Table 1.** Results for a series of tests to perturb disks near equilibrium.

type	depth	fragment?	$Q_{eff}$	notes
density	1%	no	1.01	m=4
density	1%	no	1.01	m=3
density	1%	no	1.01	m=2
height	-10%	no	1.01	
height	-2%	no	1.01	
velocity	0.50%	no	1.01	
velocity	1%	yes	1.01	
velocity	2%	yes	1.01	
velocity	10%	yes	1.01	
velocity	1%	no	1.12	
velocity	2%	no	1.12	
velocity	4%	no	1.12	
velocity	8%	no	1.12	
velocity	11%	yes	1.12	
velocity	16%	yes	1.12	

can cause a disk to fragment, but that results were fairly insensitive to perturbing the disk height or to applying small spiral density perturbations. These results are summarized in table 1.

We applied  $m = 2, 3, 4$  spiral density perturbations by multiplying the particle masses  $M_0$  by:

$$M_1 = M_0 (1 + \epsilon \cos(m\theta)) \quad (14)$$

where  $M_1$  is the perturbed particle mass and  $\epsilon$  is the depth of the perturbation, here chosen to be  $\epsilon = 0.01$ . These perturbations are similar to those done by e.g. [Boss \(2002\)](#) to seed instabilities in a grid code which does not have SPH particle noise. These perturbations were performed on the  $Q_{eff} = 1.01$  simulation and were not sufficient to force the disk to fragment.

We also wished to probe how sensitive disks are to perturbing the height. When generating ICs, there are many different methods for estimating the vertical density profile. We therefore wished to see whether perturbing a disk's scale height away from equilibrium could cause it to fragment. We ran the  $Q_{eff} = 1.01$  simulation twice, multiplying the particle  $z$  positions by 0.98 and 0.9, decreasing the scale heights by 2% and 10%, respectively. Neither of these runs fragmented.

The disks do appear to be much more sensitive to particle velocities. We applied small, axisymmetric velocity perturbations to disks which otherwise did not fragment. The perturbed velocity  $v_1$  was calculated as:

$$v_1 = v_0 \left( 1 + \epsilon \frac{R_0}{R} \right) \quad (15)$$

where  $v_0$  is the original velocity,  $R_0$  is the inner edge of the disk (where the  $\Sigma$  reaches a maximum) and  $\epsilon \ll 1$  is the depth of the perturbation. This applies a fractional perturbation of  $\epsilon$  at  $R_0$  which decays as  $1/R$ . Nearly all the disk mass lies outside of  $R_0$ .

For the  $Q_{eff} = 1.01$  disk, a 1% perturbation ( $\epsilon = 0.01$ ) was sufficient to cause fragmentation. Figure 7 shows the spiral power as a function of time for this run. Spiral power is calculated by binning  $\Sigma$  in  $(R, \theta)$  and calculating the standard deviation. The perturbed and original simulations initially develop in a similar manner for the first orbital period (defined at the most unstable radius). During this stage an

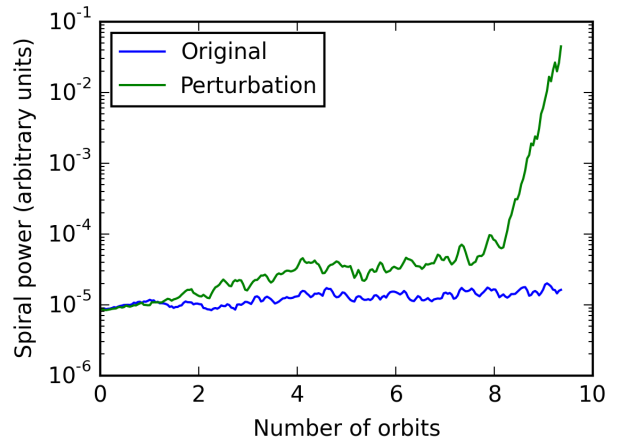


**Figure 7.** Total non-axisymmetric power versus time for a disk with and without a 1% velocity perturbation (simulation number 2). The original simulation ( $Q_{eff} = 1.01$ ) did not fragment, the simulation with a small, axisymmetric velocity perturbation does. Spiral structure initially develops similarly for both simulations for about the first orbit. For the next 8 orbits the perturbed simulation develops deeper spiral structure until it fragments after 9-10 orbits.

axisymmetric ( $m = 0$ ) density wave moves outward from the disk center. After about an orbital period the perturbed disk develops significantly more pronounced spiral density waves. After 9-10 orbits the disk fragments. Fragmentation is accompanied by a rapid spike in the spiral power as the disk becomes highly non-axisymmetric.

A similar test was performed with a much more stable disk ( $Q_{eff} = 1.12$ ). A series of perturbations were applied ( $\epsilon = .01, .02, .04, .08, .11, .16$ ). An 11% perturbation was sufficient to force the disk to fragment. Depending on the approximations used to estimate circular velocities, discrepancies on this order can happen for disks sufficiently massive to be close to the fragmentation boundary.

This demonstrates the care which must be taken in developing equilibrium models of unstable disks near the fragmentation boundary, especially with regard to the velocity calculation. An apparently small perturbation can deposit large amounts of energy in a disk, forcing it sufficiently far of equilibrium to fragment.

We also tested the importance of the inner and outer boundaries by taking a disk near the fragmentation boundary with  $Q_{eff}$  slightly above 1 and applying a step function cut-off to  $\Sigma$  on the inner edge, outer edge, and both. Waves were seen to reflect off these hard boundaries, but the effect was not sufficiently strong to drive the disk to fragmentation.

## 5 CLUMPS

The formation of tightly bound, dense clumps of gas marks the stage of disk evolution where our isothermal treatment begins to break down. We therefore restrict our analysis of clumps to the early stages of formation and limit the scope of our results.



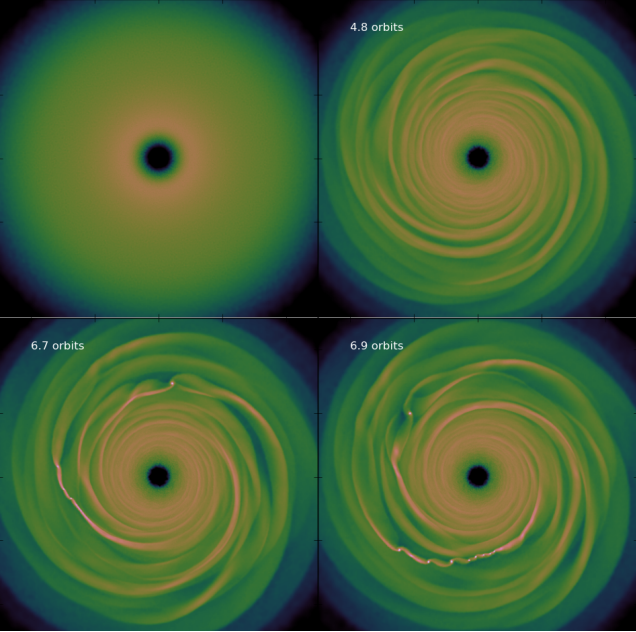


**Figure 8.** An example of the typical stages of clump formation. Clockwise, from top-left: (1) Initial conditions  $Q_{eff} < 1$  (2) Strong spiral structure develops. (3) Spiral arms become overdense and break apart into clumps. (4) The disk begins fragment strongly.

To track the formation of clumps, we developed a simple clump finding/tracking software routine<sup>4</sup> built around the group finder SKID<sup>5</sup>. To find gravitationally bound clumps, we may factor in the disk geometry. Particle masses are scaled by  $R^3$  and a density threshold is set such that at least  $N$  particles lie within the Hill-sphere of particles under consideration, where  $N$  is chosen as the number of neighbors used for SPH smoothing. This gives a threshold of

$$\rho_{min} = \frac{3NM_s}{R^3} \quad (16)$$

The SKID algorithm is then applied, which uses a friends-of-friends clustering algorithm followed by a gravitational unbinding procedure to determine which clumps are gravitationally bound. By visual inspection, this provides robust results over a large range of disk and simulation parameters, and importantly avoids marking high-density spiral arms as clumps. Figure 9 shows an example of this clump finding applied to a highly unstable PPD.

To track clumps over many time steps, clumps are first found in all simulation snapshots. They are then tracked over time by comparing clumps in adjacent time steps and seeing which have the most particles in common. Mergers (including multiple mergers), clump destruction, and clump formation are accounted for. Clump parameters such as mass, density, size, and location are all calculated and followed as a function of time.

<sup>4</sup> Our clump finding code is freely available on github at <https://github.com/ibackus/diskpy> as a part of our PPD python package *diskpy*

<sup>5</sup> SKID is freely available at <https://github.com/N-BodyShop/skid>

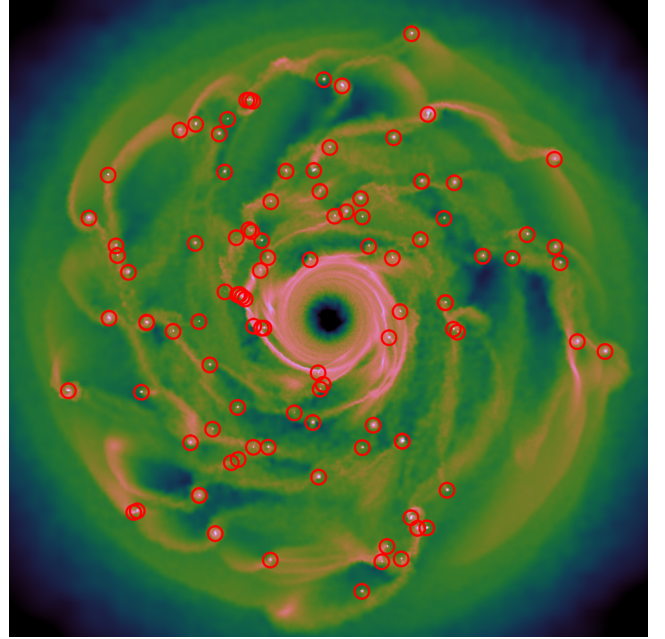


**Figure 9.** A demonstration of the clump finding algorithm used here. Integrated column density for the gas is pictured with a logarithmic color scale. Red circles mark the detected clumps. At the end of the simulation, this highly unstable disk formed 108 distinct, gravitationally bound clumps. The algorithm picks out clumps with a high success rate without reporting false positives from other high density structure such as spiral arms.

We find that clumps form according to the same general picture, as shown in figure 8. Disks with a minimum  $Q_{eff} \lesssim 1.6$  (or about  $Q_{min} \lesssim 1.3$ ) will form noticeable spiral structure after several orbital periods. Disks with an initial  $Q_{eff} < 1$  will grow overdense spiral arms which will collapse and fragment into several dense clumps. Clumps initially form near the most unstable disk radius. For these simulations, that is approximately at  $R_d$ . They form after several to tens of orbital periods at the most unstable radius. Average clump masses are around  $0.3M_{Jupiter}$ , with some rapidly growing to  $1M_{Jupiter}$ . The timescales for disk fragmentation increase rapidly as  $Q_{eff} \rightarrow 1$  (fig. 5). After this stage, the isothermal approximation begins to break down. The disks then undergo a rapid, violent fragmentation.

## 6 DISCUSSION

### 6.1 Thermodynamics

For these simulations we used a locally isothermal approximation for several reasons. We wished to perform a large scan of parameter space without compromising resolution too strongly. A computationally fast isothermal EOS is straightforward to implement. We also desired to build on previous work and to extend it to poorly studied M-dwarf systems. Our work here is directed at exploring the dependence of the fragmentation boundary on stellar/disk mass, disk height, and ICs. We leave the dependence on EOS for future work.

A non-isothermal EOS introduces non-trivial numerical

issues, especially in the context of SPH simulations of protoplanetary disks. Unwarranted, poorly understood heating terms, especially from artificial viscosity (AV), are introduced into the energy equation. Previous results (Meru & Bate 2011, 2012; Lodato & Clarke 2011; Rice et al. 2012, 2014) and our own initial tests indicate that in the context of PPDs, AV heating can dominate disk thermodynamics. Non-isothermal PPD simulations may not converge (Meru & Bate 2011), whereas in Appendix B we demonstrate that our approach does converge. It is also unclear how rapidly disks will radiatively cool, an important parameter for the possibility of disk fragmentation (Gammie 2001; Rafikov 2005, 2007). We hope to investigate these effects in future work.

The isothermal approximation used for these simulations limits the scope of our results. An isothermal EOS would well approximate a disk where stellar radiation, viscous accretion heating, and radiative losses to infinity, are nearly balanced and control the temperature of the disk. Furthermore, temperature is independent of density, which is only appropriate for an optically thin disk. The isothermal approximation applies only to scenarios where dynamical timescales are much longer than the timescales for heating/cooling back to thermal equilibrium with the background.

These conditions may not hold in the disks under consideration. This experiment therefore does not realistically follow the thermal evolution of the disk. We are limited to a preliminary investigation into the large-scale dynamics of the disk before the putative equilibrium temperature profile would be expected to be strongly altered.

During the initial stages of disk evolution, dynamical and physical timescales are of order the orbital period and disk radius, respectively. During this stage, the isothermal EOS can still provide insight into the global dynamics of a GI disk at a certain stage. However, once clumps form, the isothermal approximation no longer provides much insight. Clumps should get hot as they collapse. The dynamic timescales of dense clumps will be short as they accrete matter, decouple from the disk, and scatter with other clumps. Pressure support of clumps, which is poorly captured by an isothermal EOS, should tend to increase their size and their coupling to the disk, meaning that the violent fragmentation of disks after initial clump formation which we see in our simulations may not be the final state of a typical fragmenting disk. Clumps which are sufficiently dense may decouple from the disk enough to experience strong shocks and tidal interactions which will cause heating. These processes will strongly influence clump growth, evolution, and survival, all of which are still under investigation (Nayakshin 2010; Galvagni et al. 2012).

We therefore limit ourselves to discussing the early stages of clump formation. Our results indicate that the critical value of  $Q_{min} \lesssim 0.9$  required for fragmentation is significantly lower than some previous results which found closer to  $Q_{min} \lesssim 1.5$ . Although this makes requirements for fragmentation more stringent, it does not rule out GI and disk fragmentation as important mechanisms during planet formation in PPDs around M-dwarfs.

## 6.2 Previous results

We find that for most disks,  $Q \lesssim 0.9$  is required for disk fragmentation. Re-parameterizing  $Q$  as  $Q_{eff}$  to include the stabilizing effect of disk height provides a more precise way to predict fragmentation. The ratio of  $Q_{eff}/Q$  can vary by 30% for reasonable disk parameters. This ratio will vary even more when considering solar type stars in addition to M-dwarfs. However,  $Q$  still provides a reasonable metric for disk fragmentation.

Other isothermal studies have found different boundaries. In contrast to our results, Nelson et al. (1998) found the threshold to be  $Q \leq 1.5$ . Boss (1998) found  $Q$  as high as 1.3 would fragment. Boss (2002) found, using an isothermal EOS or diffusive radiative transfer, that  $Q = 1.3 - 1.5$  would fragment. Mayer et al. (2004) found  $Q = 1.4$  isothermal disks would fragment. Pickett et al. (2003) found that cooling a disk from  $Q = 1.8$  to  $Q = 0.9$  caused it to fragment. Their clumps did not survive, although as they note that may be due to numerical issues. Boley (2009) found that disks could be pushed below  $Q = 1$  by mass loading and still not fragment, by transporting matter away from the star and thereby decreasing  $\Sigma$  and increasing  $Q$ . It should be noted that some of these simulations were run at much lower resolution than ours. Differences may also be due in part to simulation methods: using cylindrical grids, spherical grids, or SPH methods; applying perturbations; or even 2D (Nelson et al. 1998) vs 3D simulations.

Since all the details of previous work are not available, the source of the discrepancy in critical  $Q$  values is uncertain. One source of discrepancy is simply how  $Q$  is calculated. As mentioned in §4, approximating  $Q$  by ignoring disk self-gravity and pressure forces can overestimate  $Q$  on the 10% level for heavy disks.

The discrepancy may also be due to the different methods of constructing equilibrium disks. As demonstrated in §4.1, overestimating velocities at less than the percent level can force a disk to fragment. Disks near the fragmentation boundary are very sensitive to ICs. Initial conditions are not in general available for previous work, however we can note that some studies appear to display a rapid evolution of  $Q$  at the beginning of the simulation. For example, some runs of Pickett et al. (2003) evolve from  $Q_{min} = 1.5$  to  $Q_{min} = 1$  in fewer than 3 ORPs (see their Figure 14). Figure 1 of Mayer et al. (2004) shows two isothermal simulations which evolve from a  $Q_{min}$  of 1.38 and 1.65 to  $Q_{min} = 1$  in fewer than 2 ORPs. This is indicative of ICs which are out of equilibrium.

In contrast, even our very unstable disks display a remarkably smooth and gradual initial evolution. Figure 10 shows the behavior of the minimum  $Q_{eff}$  (normalized by its initial value) for our fragmenting runs as a function of time until fragmentation. For all the runs,  $Q_{eff}$  decreases gradually for most of the simulation until dropping rapidly shortly before the disk fragments. For our runs near the fragmentation boundary, this is much more gradual and much less pronounced than for the runs of Pickett et al. (2003) or Mayer et al. (2004) mentioned above. For us, a much smaller change in  $Q$  takes around 10 ORPs.  $Q_{eff}$  evolves even more slowly for non-fragmenting runs.  $Q_{min}$  follows a similar behavior, although with more scatter (in large part because  $Q$  does not determine the timescale until fragmentation as well as  $Q_{eff}$  does).

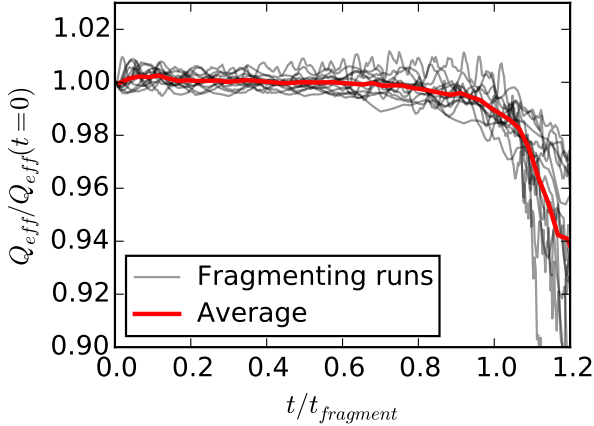


**Figure 10.** Minimum  $Q_{eff}$  normalized by the initial minimum  $Q_{eff}$  vs fraction of time until fragmentation for all the fragmenting runs. The average of these runs is plotted in red. Disk fragmentation occurs at  $t/t_{fragment} = 1$ . All runs follow similar trajectories in this plot, even though a significant range of initial  $Q_{eff}$  and  $t_{fragment}$  values are represented here (all the fragmenting runs in Fig. 5 are presented here). The simulations undergo an initially gradual decrease in  $Q_{eff}$  which steepens sharply shortly before fragmentation.

However it is not certain how close to equilibrium ICs should be to capture the relevant physics of PPDs. Actual disks are constantly evolving from the early stages of star formation until the end of the disk lifetime. We chose to use disks as close to equilibrium as possible, seeded only with SPH poisson noise, to avoid introducing numerical artifacts. Some authors introduce density perturbations which are controllable. If sufficiently large, they may serve to ameliorate the problems mentioned above by explicitly having fragmentation be driven by physically reasonable spiral modes (e.g. Boss (2002)) or intentionally large random perturbations (e.g. Boley (2009)). Others have considered mass loading as a means to grow to low  $Q$  (Boley 2009).

### 6.3 GI in PPDs

Observed disks around M-dwarfs do not appear to have low enough inferred  $Q_{min}$  values to be sufficiently unstable for fragmentation under GI, however this is what would be expected given the short timescales for the fragmentation of an unstable disk. Reported disk ages are of order  $10^6$  years (Haisch et al. 2001), orders of magnitude longer than fragmentation timescales, making the observation of a highly gravitationally unstable disk unlikely. This is a strong selection effect for observed disk parameters.

Although fragmentation timescales are very rapid, disks may persist much longer in moderately unstable configurations where GI drives large scale structure but which have not grown sufficiently unstable as to be prone to fragmentation. Early work is being done on trying to observe GI driven structures, but with current instrumentation such structures will be difficult to resolve (Douglas et al. 2013; Evans et al. 2015).

As shown in figure 6, the fiducial values for disk param-

eters adopted here place observed disks near the boundary for fragmentation. The fact that observations indicate normal disk parameters which are close to the boundary, rather than orders of magnitude off, suggests it is plausible that a significant portion of PPDs around M-dwarfs will undergo fragmentation. This would predict a sharp transition in the distribution of inferred  $Q_{eff}$  values around  $Q_{eff} = 1$ . Older disks tend to expand radially (Isella et al. 2009), thereby decreasing  $\Sigma$ , increasing  $Q$ , and pushing them away from the  $Q_{eff} = 1$  boundary. We note that while  $Q$  is a reasonably strong predictor of fragmentation, disk height is an additional parameter worth measuring to predict fragmentation.

Given the results of these isothermal simulations, we expect GI to play a large role in the early stages of planet formation around M-dwarfs. The exact role of star mass/type on fragmentation remains unclear. The parameter space we scanned is sufficiently large that adding an extra dimension was prohibitive, we therefore only studied one star mass. Future work should be able to determine what stars are the most suitable for fragmentation. Once large-scale density perturbations are formed via GI, the fate of the disk remains unclear. Future work should include more sophisticated thermodynamics to follow the evolution of the gaseous component of the disk to better determine under what conditions clumps will form, and what is required for them to survive. Additionally, decreasing the resolution in our isothermal SPH simulations appears to drive fragmentation (see §B). The importance of resolution in simulations is subject to much investigation and should be further pursued (e.g. Meru & Bate (2011, 2012); Cartwright et al. (2009b)).

Planet formation will of course require the concentration of solids as well. Including dust in simulations of young PPDs will be required. In a fully 3D, highly non-axisymmetric environment, we may investigate how GI affects solids. Dust enhancement through pressure gradients, dust evolution through collisions and coagulation, and dust coupling to disk opacity and cooling, will all strongly affect prospects for planet formation. Dust dynamics in PPDs using SPH has been proposed recently (Laibe & Price 2012; Price & Laibe 2015), and we hope to explore solid/gas interactions in the future.

### CODE AND DATA

The code repository for generating our ICs and for clump-tracking is freely available online at <https://github.com/ibackus/diskpy> as a part of our *diskpy* python package. IC generation is contained within the subpackage *diskpy.ICgen* and clump tracking is contained within the subpackage *diskpy.clumps*. A public version of ChaNGa is available at <http://www-hpcc.astro.washington.edu/tools/changa.html> and is required for IC generation. The group finding software SKID (required for clump finding) is available at <https://github.com/N-BodyShop/skid> and depends also on tipsy tools ([https://github.com/N-BodyShop/tipsy\\_tools](https://github.com/N-BodyShop/tipsy_tools)).

We have also made much of our data available online at the University of Washington’s ResearchWorks archive at <http://hdl.handle.net/1773/34933>. Initial conditions and final simulation snapshots are available for all the simu-

lations presented here. Wengen test results (see appendix A) are also available there.

## ACKNOWLEDGEMENTS

We would like to acknowledge Aaron Boley for many fruitful discussions and much feedback on this work. We thank David Fleming for help on this work and *diskpy*. This work was performed as part of the NASA Astrobiology Institute's Virtual Planetary Laboratory, supported by the National Aeronautics and Space Administration through the NASA Astrobiology Institute under solicitation NNH12ZDA002C and Cooperative Agreement Number NNA13AA93A. The authors were also supported by NASA grant NNX15AE18G. This work used the Extreme Science and Engineering Discovery Environment (XSEDE)(Towns et al. 2014), which is supported by National Science Foundation grant number ACI-1053575. This work was facilitated through the use of advanced computational, storage, and networking infrastructure provided by the Hyak supercomputer system at the University of Washington.

## REFERENCES

- Adams F. C., Ruden S. P., Shu F. H., 1989, *ApJ*, **347**, 959  
 Andrews S. M., Williams J. P., 2005, *ApJ*, **631**, 1134  
 Andrews S. M., Wilner D. J., Hughes A. M., Qi C., Dullemond C. P., 2009, *ApJ*, **700**, 1502  
 Apai D., Pascucci I., 2009, *Meteoritics and Planetary Science Supplement*, **72**, 5361  
 Apai D., Pascucci I., 2010, in *Astrobiology Science Conference 2010: Evolution and Life: Surviving Catastrophes and Extremes on Earth and Beyond*. p. 5396  
 Balsara D. S., 1995, *Journal of Computational Physics*, **121**, 357  
 Barnes J., Hut P., 1986, *Nature*, **324**, 446  
 Binney J., Tremaine S., 1987, *Galactic dynamics*  
 Boley A. C., 2009, *ApJ*, **695**, L53  
 Boley A. C., Durisen R. H., 2010, *ApJ*, **724**, 618  
 Borucki W. J., et al., 2010, *Science*, **327**, 977  
 Boss A. P., 1997, *Science*, **276**, 1836  
 Boss A. P., 1998, *ApJ*, **503**, 923  
 Boss A. P., 2002, *ApJ*, **576**, 462  
 Boss A. P., 2006a, *ApJ*, **643**, 501  
 Boss A. P., 2006b, *ApJ*, **644**, L79  
 Boss A. P., 2008, *Physica Scripta Volume T*, **130**, 014020  
 Cameron A. G. W., 1978, *Moon and Planets*, **18**, 5  
 Cartwright A., Stamatellos D., Whitworth A. P., 2009a, *MNRAS*, **395**, 2373  
 Cartwright A., Stamatellos D., Whitworth A. P., 2009b, *MNRAS*, **395**, 2373  
 Chiang E. I., Goldreich P., 1997, *ApJ*, **490**, 368  
 Douglas T. A., Caselli P., Ilee J. D., Boley A. C., Hartquist T. W., Durisen R. H., Rawlings J. M. C., 2013, *MNRAS*, **433**, 2064  
 Durisen R. H., Boss A. P., Mayer L., Nelson A. F., Quinn T., Rice W. K. M., 2007, *Protostars and Planets V*, pp 607–622  
 Evans M. G., Ilee J. D., Boley A. C., Caselli P., Durisen R. H., Hartquist T. W., Rawlings J. M. C., 2015, *MNRAS*, **453**, 1147  
 Galvagni M., Hayfield T., Boley A., Mayer L., Roškar R., Saha P., 2012, *MNRAS*, **427**, 1725  
 Gammie C. F., 2001, *ApJ*, **553**, 174  
 Hachisu I., 1986, *ApJS*, **61**, 479  
 Haghighipour N., Boss A. P., 2003, *ApJ*, **598**, 1301  
 Haisch Jr. K. E., Lada E. A., Lada C. J., 2001, *ApJ*, **553**, L153  
 Han E., Wang S. X., Wright J. T., Feng Y. K., Zhao M., Fakhouri O., Brown J. I., Hancock C., 2014, *PASP*, **126**, 827  
 Helled R., et al., 2014, in *Beuther H., Klessen R. S., Dullemond C. P., Henning T., eds., Protostars and Planets VI*. University of Arizona Press, pp 643–665, doi:10.2458/azu\_uapress\_9780816531240  
 Isella A., Carpenter J. M., Sargent A. I., 2009, *ApJ*, **701**, 260  
 Laibe G., Price D. J., 2012, *MNRAS*, **420**, 2345  
 Lodato G., Clarke C. J., 2011, *MNRAS*, **413**, 2735  
 Lynden-Bell D., Pringle J. E., 1974, *MNRAS*, **168**, 603  
 Mann R. K., Andrews S. M., Eisner J. A., Williams J. P., Meyer M. R., Di Francesco J., Carpenter J. M., Johnstone D., 2015, *ApJ*, **802**, 77  
 Mayer L., Gawryszczak A. J., 2008, in *Fischer D., Rasio F. A., Thorsett S. E., Wolszczan A., eds, Astronomical Society of the Pacific Conference Series Vol. 398, Extreme Solar Systems*. p. 243 (arXiv:0710.3590)  
 Mayer L., Quinn T., Wadsley J., Stadel J., 2004, *ApJ*, **609**, 1045  
 Menon H., Wesolowski L., Zheng G., Jetley P., Kale L., Quinn T., Governato F., 2015, *Computational Astrophysics and Cosmology*, **2**, 1  
 Meru F., Bate M. R., 2011, *MNRAS*, **411**, L1  
 Meru F., Bate M. R., 2012, *MNRAS*, **427**, 2022  
 Monaghan J. J., 1992, *ARA&A*, **30**, 543  
 Nayakshin S., 2010, *MNRAS*, **408**, L36  
 Nelson A. F., 2006, *MNRAS*, **373**, 1039  
 Nelson A. F., Benz W., Adams F. C., Arnett D., 1998, *ApJ*, **502**, 342  
 Paardekooper S.-J., 2012, *MNRAS*, **421**, 3286  
 Pickett B. K., Mejía A. C., Durisen R. H., Cassen P. M., Berry D. K., Link R. P., 2003, *ApJ*, **590**, 1060  
 Pollack J. B., Hubickyj O., Bodenheimer P., Lissauer J. J., Podolak M., Greenzweig Y., 1996, *Icarus*, **124**, 62  
 Price D. J., Laibe G., 2015, *MNRAS*, **451**, 813  
 Rafikov R. R., 2005, *ApJ*, **621**, L69  
 Rafikov R. R., 2007, *ApJ*, **662**, 642  
 Rice W. K. M., Forgan D. H., Armitage P. J., 2012, *MNRAS*, **420**, 1640  
 Rice W. K. M., Paardekooper S.-J., Forgan D. H., Armitage P. J., 2014, *MNRAS*, **438**, 1593  
 Rogers P. D., Wadsley J., 2011, *MNRAS*, **414**, 913  
 Romeo A. B., Burkert A., Agertz O., 2010, *MNRAS*, **407**, 1223  
 Seager S., Dalcanton J. J., Postman M., Tumulson J., Mather J. C., 2015, preprint, (arXiv:1511.01144)  
 Shu F. H., Tremaine S., Adams F. C., Ruden S. P., 1990, *ApJ*, **358**, 495  
 Toomre A., 1964, *ApJ*, **139**, 1217  
 Towns J., et al., 2014, *Computing in Science and Engineering*, **16**, 62  
 Vorobyov E. I., 2011, *ApJ*, **729**, 146  
 Wadsley J. W., Stadel J., Quinn T., 2004, *New Astronomy*, **9**, 137

## APPENDIX A: WENGEN TESTS

The Wengen tests are a series of code tests designed to compare different astrophysical hydrodynamic and gravity simulation codes and are available online at <http://www.astrosim.net/code/>. We ran Wengen test 4, an unstable isothermal PPD, with ChaNGa. We present the results of our simulation here. We find that our results are in good agreement with other simulation codes (previous test results can be found at <http://users.camk.edu.pl/gawrysz/test4/>). We have reproduced all the plots on the Wengen test website for the ChaNGa results, which are available at <http://hdl>.

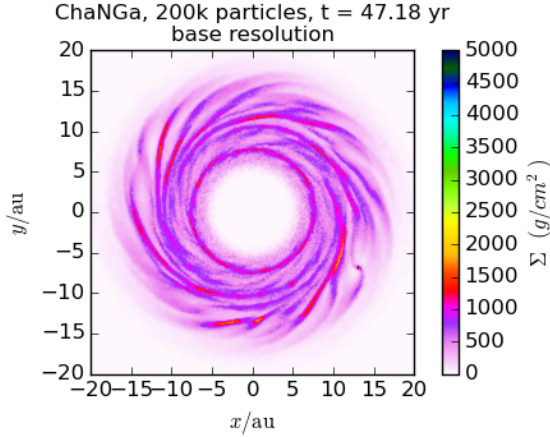


**Figure A1.** Surface density map of the Wengen test simulation at  $t = 47.18$  years (6 in code units). This reproduces the *surface density map* at  $t = 6$  in the images table at <http://users.camk.edu.pl/gawrysz/test4/#images>. As with the other SPH codes and the higher resolution runs, a clump has formed.

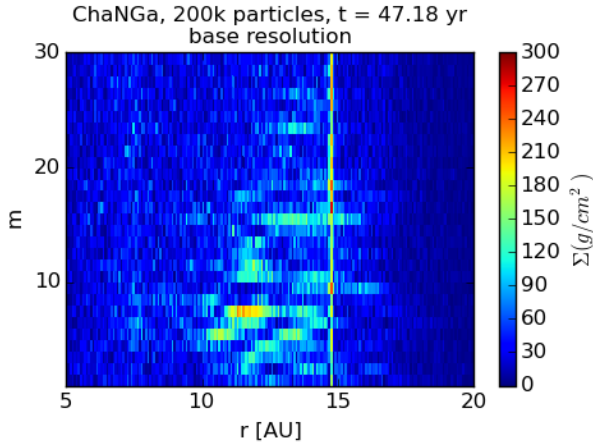


**Figure A2.** Amplitude of the fourier transform of the surface density along the angular direction as a function of radius, for the same snapshot in figure A1. This reproduces the *FFT of surface density* plots at  $t = 6$  in the images table at <http://users.camk.edu.pl/gawrysz/test4/#images>. The clump which has formed shows up as a bright vertical stripe. 200 radial bins were used. The features in the plot agree well with those for other SPH codes and the high resolution codes.

[handle.net/1773/34933](https://doi.org/10.1093/mnras/stw271). Our ICs are the 200k-particle run. Here we present a few figures demonstrating the ChaNGa results.

## APPENDIX B: CONVERGENCE TEST

Previous work has indicated that the results of SPH simulations of PPDs can be resolution dependent (Lodato & Clarke 2011; Meru & Bate 2011, 2012). Nelson (2006) laid out several resolution requirements for SPH simulations of

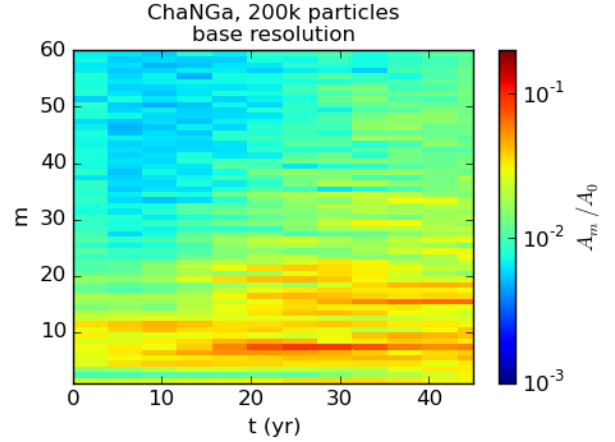


**Figure A3.** Radially integrated fourier transform of surface density as a function of time. The amplitudes are normalized by the DC amplitude (not shown). This reproduces the *FFT integrated over  $r$ ,  $A_m(t)$*  plots in the images tables available at <http://users.camk.edu.pl/gawrysz/test4/#images>. The development of strong power around  $m = 8$  and later around  $m = 16$  agrees with other codes.

PPDs. For our suite of simulations, we exceed the mass resolution requirement by a minimum factor of 7, and most simulations exceed it by a factor of 40. We also easily meet their scale height resolution requirement. At the midplane of the most unstable disk radius, the ratio of the smoothing length to the scale height is between 4 – 12 for all our runs (Nelson (2006) finds this ratio should be at least  $\sim 4$ ).

As part of our analysis, we ran a basic convergence test to verify our simulation code and to investigate the effects of resolution on disk fragmentation in SPH simulations. We ran a simulation close to the fragmentation boundary with a minimum  $Q_{eff} = 1.06$  (simulation 48 in table B2) at 6 different resolutions from 50k to 10M particles. These runs are summarized in table B1.

We find (i) that low resolution simulations are more susceptible to disk fragmentation and (ii) that simulations appear to converge reasonably well, with our chosen resolution of  $10^6$ -particles being sufficient for the analysis presented in this paper. However, these convergence tests are only preliminary and future work may reveal that higher particle count is required for fully believable results. Convergence may also depend on EOS, cooling prescriptions, and whether a grid code or an SPH code is used.

Figure B1 shows logarithmic surface density plots of all 6 runs after 4.0 ORPs. The 50k- and 100k-particle runs have already fragmented violently. The 500k-particle run has developed somewhat stronger spiral power than the higher resolution runs and eventually fragments after about 12 ORPs. The other runs have developed some spiral power that is insufficient to drive the disks to fragmentation.

Figure B2 shows what we call the normalized spiral power. We calculate spiral power by binning the surface density in  $R, \theta$  (we used  $128 \times 128$  bins here), calculating the standard deviation along the angular direction, and summing along the radial direction. We then normalize by multiplying the spiral power by  $\sqrt{N}$ , where  $N$  is the number of

**Table B1.** Table of convergence tests runs. ICs are identical to simulation 48 in table B2 but with a different number of particles. The resolution is the number of SPH particles in the run. Runs that fragment are highly non-axisymmetric, so the quoted  $Q_{eff}$  values are only illustrative. Runs that don't fragment approach a stable value significantly above 1.

Run	Resolution	Fragment?	Final $Q_{eff}$
0	50k	yes	0.67
1	100k	yes	0.69
2	500k	yes	0.89
3	1M	—	1.11
4	5M	—	1.11
5	10M	—	1.12

SPH particles in the run. This is done to account for noise in the number of particles per bin which scales as  $\propto 1/\sqrt{n_{per\ bin}}$  where  $n_{per\ bin}$  is approximately proportional to  $N$ .

The normalized spiral power then represents how much larger than the particle noise the spiral power is. Fragmentation is visible in figure B2 as a sharp rise in power at the end of the simulation. As can be seen, the normalized spiral power decreases with increasing particle count and converges for the higher-resolution simulations.

As expected for  $Q_{eff} = 1.06$ , the higher resolution simulations do not fragment. As shown in table B1, the simulations with  $N \geq 10^6$  particles approach a stable value of  $Q_{eff} \approx 1.11$  and therefore would not fragment if run for longer. Simulations with  $N \leq 500k$  particles approached very low  $Q_{eff}$  minimum values, although  $Q_{eff}$  is strictly speaking not well defined for highly non-axisymmetric disks.

Surface density after 4.0 ORPs

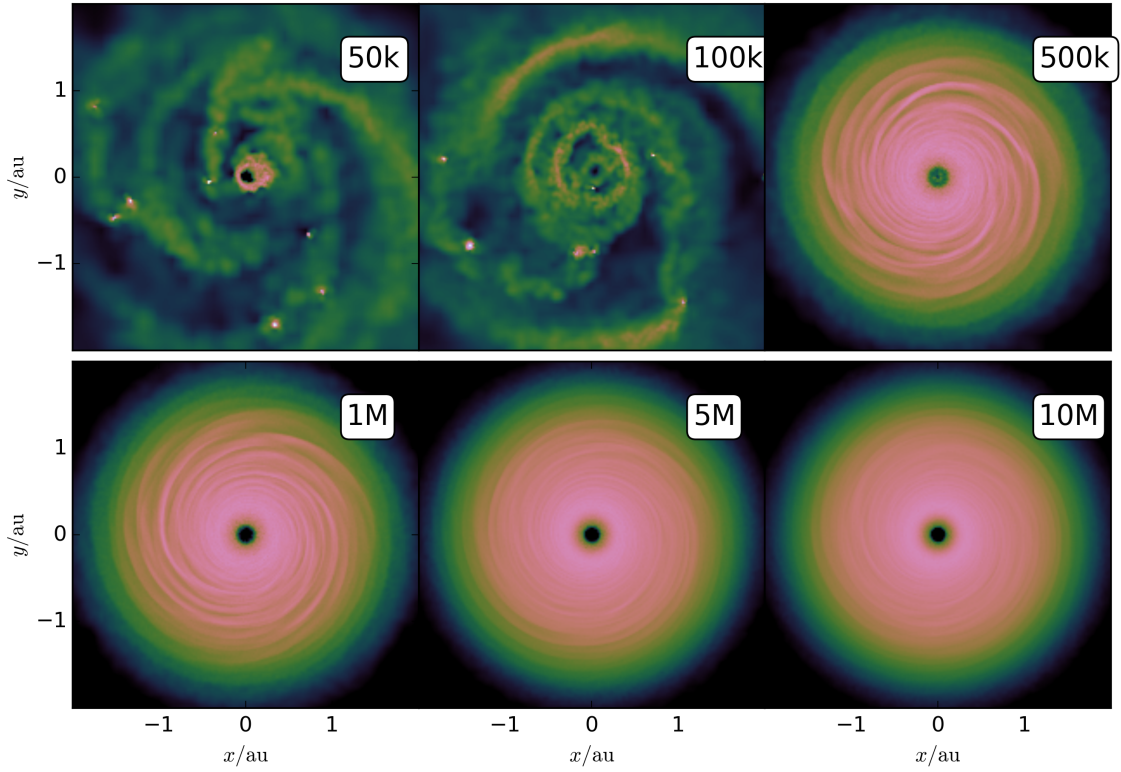


**Figure B1.** Logarithmic surface density plots for the simulations listed in table B1 of a  $Q_{eff} = 1.06$  run after 4.0 ORPs (defined at the initial disk radius). The low resolution runs have already fragmented. The 500k-particle run has developed strong spiral power and will eventually fragment. The remaining runs do not fragment and approach a value of  $Q_{eff} > 1.1$  within the course of the simulations.

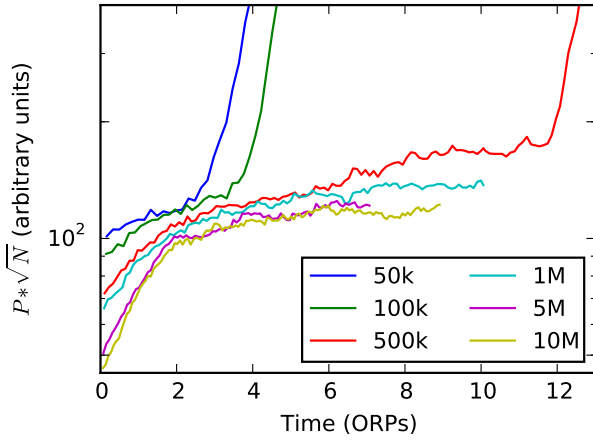


**Figure B2.** Normalized spiral power vs. time for the 6 simulations in the convergence test. Power is calculated by binning  $\Sigma$  in  $(R, \theta)$ , calculating the standard deviation along  $\theta$  and summing along  $R$ . Power is then normalized by multiplying by  $\sqrt{N}$  to adjust for the power in particle noise. Fragmentation is seen for the simulations with 50k-, 100k-, and 500k-particles as a rapid increase in spiral power at the end of the simulation. As expected, the higher resolution simulations do not fragment.



This paper has been typeset from a  $\text{T}_\text{E}\text{X}/\text{L}^\text{A}\text{T}_\text{E}\text{X}$  file prepared by the author.

**Table B2.** The suite of runs presented here.

Sim.	Profile	$R_d$ (AU)	$T_0$ (K)	$M_d$ ( $M_\odot$ )	$Q$	$Q_{eff}$	fragment?
0	powerlaw	1/3	64	0.02	0.78	0.76	yes
1	powerlaw	3	64	0.03	0.82	0.86	yes
2	powerlaw	30	64	0.04	0.88	1.01	—
3	powerlaw	1/3	129	0.03	0.81	0.84	yes
4	powerlaw	3	129	0.04	0.86	0.96	yes
5	powerlaw	30	129	0.06	0.92	1.12	—
6	powerlaw	1/3	258	0.04	0.85	0.93	yes
7	powerlaw	3	258	0.06	0.91	1.07	—
8	powerlaw	30	258	0.09	0.98	1.26	—
9	powerlaw	1/3	64	0.01	0.95	0.94	yes
10	powerlaw	3	64	0.02	0.99	1.05	—
11	powerlaw	30	64	0.04	1.04	1.23	—
12	powerlaw	1/3	129	0.02	0.98	1.03	—
13	powerlaw	3	129	0.03	1.02	1.16	—
14	powerlaw	30	129	0.05	1.09	1.35	—
15	powerlaw	1/3	258	0.03	1.01	1.13	—
16	powerlaw	3	258	0.04	1.07	1.29	—
17	powerlaw	30	258	0.07	1.12	1.48	—
18	powerlaw	1/3	64	0.01	1.12	1.12	—
19	powerlaw	3	64	0.02	1.15	1.25	—
20	powerlaw	30	64	0.03	1.21	1.45	—
21	powerlaw	1/3	129	0.02	1.14	1.22	—
22	powerlaw	3	129	0.03	1.19	1.37	—
23	powerlaw	30	129	0.04	1.24	1.56	—
24	powerlaw	1/3	258	0.02	1.18	1.33	—
25	powerlaw	3	258	0.04	1.23	1.51	—
26	powerlaw	30	258	0.06	1.27	1.7	—
27	powerlaw	1/3	64	0.01	1.28	1.3	—
28	powerlaw	3	64	0.02	1.32	1.45	—
29	powerlaw	30	64	0.03	1.37	1.67	—
30	powerlaw	1/3	129	0.01	1.31	1.41	—
31	powerlaw	3	129	0.02	1.35	1.59	—
32	powerlaw	30	129	0.04	1.4	1.78	—
33	powerlaw	1/3	258	0.02	1.34	1.54	—
34	powerlaw	3	258	0.03	1.39	1.73	—
35	powerlaw	30	258	0.05	1.42	1.93	—
36	powerlaw	1	64	0.02	0.8	0.81	yes
37	powerlaw	9	64	0.03	0.84	0.92	yes
38	powerlaw	1	129	0.03	0.83	0.89	yes
39	powerlaw	9	129	0.05	0.89	1.03	—
40	powerlaw	1	258	0.04	0.87	0.99	—
41	powerlaw	9	258	0.07	0.94	1.15	—
42	powerlaw	1/3	64	0.02	0.87	0.85	yes
43	powerlaw	1	64	0.02	0.88	0.9	yes
44	powerlaw	3	64	0.02	0.9	0.96	yes
45	powerlaw	9	64	0.03	0.93	1.02	—
46	powerlaw	30	64	0.04	0.96	1.12	—
47	powerlaw	1/3	129	0.02	0.89	0.93	yes
48	powerlaw	1	129	0.03	0.92	0.99	—
49	powerlaw	3	129	0.04	0.94	1.06	—
50	powerlaw	9	129	0.04	0.97	1.14	—
51	powerlaw	30	129	0.06	1.0	1.23	—
52	powerlaw	1/3	258	0.03	0.93	1.03	—
53	powerlaw	1	258	0.04	0.96	1.1	—
54	powerlaw	3	258	0.05	0.99	1.18	—
55	powerlaw	9	258	0.06	1.02	1.27	—
56	powerlaw	30	258	0.08	1.06	1.38	—
57	viscous	5	129	0.04	0.91	1.01	yes
58	viscous	9	129	0.04	1.0	1.13	—
59	viscous	11	129	0.04	1.04	1.19	—
60	viscous	13	129	0.04	1.09	1.26	—
61	viscous	16	129	0.04	1.13	1.32	—
62	viscous	19	129	0.04	1.17	1.38	—
63	viscous	27	129	0.04	1.25	1.51	—